# NMR at Cryogenic Temperatures: A $^{13}C$ NMR Study of Ferrocene

**Anita M. Orendt, Julio C. Facelli,† Yi Jin Jiang, and David M. Grant***

*Department of Chemistry and Center for High Performance Computing, University of Utah, Salt Lake City, Utah 84112*

*Received: February 11, 1998; In Final Form: June 8, 1998*

A new cryogenic apparatus is described that can be used to obtain NMR spectra at temperatures down to 8−10 K. The static solid $^{13}C$ NMR spectrum of ferrocene is recorded at that temperature. Spectra recorded at higher temperatures show that ferrocene is still freely rotating about its 5-fold symmetry axis on the $^{13}C$ NMR time scale at 45−50 K. A comparison of the principal values of the $^{13}C$ chemical-shift tensor obtained from the room- and low-temperature spectra of ferrocene indicates that the lowest frequency chemical shift principal component, $\delta_{33}$, is tilted off this symmetry axis by approximately 12°. Quantum chemical calculations of the chemical-shift tensor, completed on structures of ferrocene from the literature as well as on optimized structures with the cyclopentadienyl rings locked in both the staggered and eclipsed arrangements, predict the angle between the $\delta_{33}$ direction and the rotation axis to be between 11° and 15°, depending upon the geometry used in the calculation. The calculations also predict the sign of the angular perturbation, information not obtained from the experiment. An explanation of this angular change in the $\delta_{33}$ direction is provided by the composition of the molecular orbitals.

## Introduction

There are numerous reasons to perform solid-state NMR experiments at cryogenic temperatures. At these temperatures a large increase in sensitivity due to the Boltzmann factor exists. Additionally, most molecular motions, which lead to averaging of the principal values obtained from a static powder pattern, are stopped. Finally, the low temperatures allow for the study of species that are isolated or trapped in an inert gas matrix.

Our first apparatus for obtaining static solid-state NMR spectra at cryogenic temperatures was described by Zilm et al. in 1980.[1] Since then, several other cryogenic devices capable of obtaining static spectra at temperatures below 30 K have been described.[2,3,4] In addition, several MAS probes capable of obtaining spectra at temperatures below 77 K have also been described.[5,6] The equipment used for obtaining static spectra are divided into those that keep the rf coil at room temperature[1,3] and those that have the rf coil in the low-temperature region.[2,4] Examples of the first type utilize closed-cycle helium refrigeration systems that have bottom temperatures in the vicinity of 25 K. There are, however, instances where this is not cold enough to stop molecular motions and/or keep a reactive species for the period of time necessary to obtain NMR spectra. The latter systems are based on helium transfer cryogenic systems and as such can reach much lower temperatures. These are only capable of keeping a sample cold for a period of about 24−48 h; moreover, they are more expensive to use due to their high rates of helium consumption.

In more recent years, closed-cycle cryogenic systems capable of temperatures as low as 4 K have become commercially available, making it possible to maintain a sample at these temperatures for much longer periods of time. In this paper, we describe how our 1.9 T electromagnet system[1] has been modified to work with this newer cryostat on a 4.7 T Oxford horizontal bore superconducting magnet. The use of a horizontal bore magnet instead of a standard vertical bore magnet simplifies the insertion of the cryogenic sample and the associated probe. The change from an electromagnet to a superconducting magnet requires a saddle design for the rf sample coil, which operates at room temperature. Unfortunately, the saddle coil is much less efficient in terms of power requirements than a solenoid coil of the same inductance. Moving to a higher magnetic field results in higher sensitivity, as well as some increase in resolution, i.e., the spread of the chemical shift scale is increased and, therefore, features obscured by overlapping bands at the lower field may be resolved. In this paper, the cryogenic setup, including the probe, is described and the application of the equipment to the study of ferrocene is presented.

At room temperature, the ferrocene molecule is rapidly rotating about its 5-fold symmetry axis. The activation barrier to this rotation has been estimated by $^1H$ NMR studies to be between 5.4 and 24.8 kJ/mol, depending on which of the three solid-state phases of ferrocene is present.[7] As a result of this motion, the powder pattern obtained at room temperature is axially symmetric with the unique component ($\delta_{||}$) along the axis of rotation. The remaining two degenerate components ($\delta_{\perp}$) are in the plane perpendicular to the axis of rotation. The principal values at room temperature have been previously measured.[8,9] At lower temperatures, the powder pattern is defined by three different components, $\delta_{11}$, $\delta_{22}$, and $\delta_{33}$, indicating that the rapid rotation of the molecule either has been slowed on the NMR time scale or has stopped. The principal values from these two spectra are used to calculate the orientation of the principal values in the molecular frame. Theoretical calculations of the shift tensor support both the assumptions needed to determine the orientation of the tensor as well as the actual principal values.

† Center for High Performance Computing.

S1089-5639(98)01079-2 CCC: $15.00 
Published on Web 09/09/1998

## Experimental Section

**Sample**. Ferrocene (Aldrich) was sublimed before use. Several freeze−pump−thaw cycles were completed to remove air from the sample before the cryostat was cooled to the bottom temperature. The ferrocene was held at room temperature and vapor-deposited onto the cold sapphire tip. Spectra were recorded at the bottom temperature of the cryostat; the temperature was then increased until the spectra indicated that the ferrocene molecule was beginning to rotate. The actual temperature of the sample was estimated to be within 2 K of the reported value, and the temperature was stable to ±1 K over the length of the NMR measurement. Spectra of the deposited ferrocene were also recorded at 70 K and at room temperature; the line shapes of these spectra were identical to those obtained for room-temperature ferrocene held in a normal NMR sample tube. External referencing was completed by placing a cell of TMS in the coil and inserting the probe and cryostat into the magnet. All spectra were transferred to a VAX computer for processing and spectral fitting.

**Cryogenic and NMR Equipment.** The cryogenic equipment consists of a RMC Cryosystems LTS-1C-4.5 closed-cycle refrigeration system. The cryostat, a three-stage water-cooled unit with a Joule−Thomson loop, has a bottom temperature of 3.6 K and a heat capacity of about 1.5 W at 4.2 K. Silicon diodes are mounted on each of the three stages, and a gallium−aluminum−arsenide diode (GaAlAs) and a resistive heater are mounted at the end of the coldfinger. The system can be operated at any temperature between the bottom temperature and room temperature with the use of a RMC Cryosystems Series 4000 cryogenic thermometer/controller. Control of the temperature can be based on the temperature at any of the three silicon diodes; no control based on the GaAlAs diode is available.

The coldfinger portion of this system, equipped for the NMR experiment, is shown in Figure 1. A 7 in. long, 0.25 in. diameter rod constructed of oxygen-free high-conductivity (OFHC) copper is mounted to the cryostat via a threaded fitting. Good thermal contact between the cold head and the copper rod is maintained with the use of an indium gasket. A 3.5 in. long, 0.094 in. diameter sapphire rod is fitted into the end of the copper rod using indium solder. The sapphire rod has a pointed tip to allow for a better filling factor in the sample region. The temperature at the sapphire rod is estimated to be 8−10 K based on the observation that a pure neon matrix will start to deposit on the cold tip at its lowest temperature.

The vacuum shroud over the cold head consists of a two-part system. The first two stages have both an internal heat shield as well as a nonmagnetic stainless steel shroud. The heat shield and the metal shroud cover all but the sapphire rod and the last several inches of the copper rod. A glass shroud, consisting of 0.75 in. glass fitted with a section of a 10 mm NMR tube and then 0.25 in. glass tubing, couples to the bottom of the metal shroud via a 0.75 in. Cajon fitting. This glass shroud maintains the thermal isolation of the sample region as well as provides the means for attaching the cryogenic cold head with a Cajon fitting to either a vacuum line or other glassware for sample introduction.

The probe is home-built and consists of a single 11 mm diameter saddle coil that is doubly tuned to both the $^{13}C$ and $^{1}H$ frequencies. The electronic circuit used has been described previously.[10] A Hartmann−Hahn match with a proton 90° pulse of about 5.3 $\mu$s is achieved using approximately 530 W of $^{13}C$ power and 180 W of $^{1}H$ power. This match is limited by the $^{13}C$ power the probe electronics can withstand. However, a higher decoupling field strength can be achieved by increasing the $^{1}H$ power by 3 dB during the decoupling period, resulting in a decoupling field estimated to be 65 kHz.

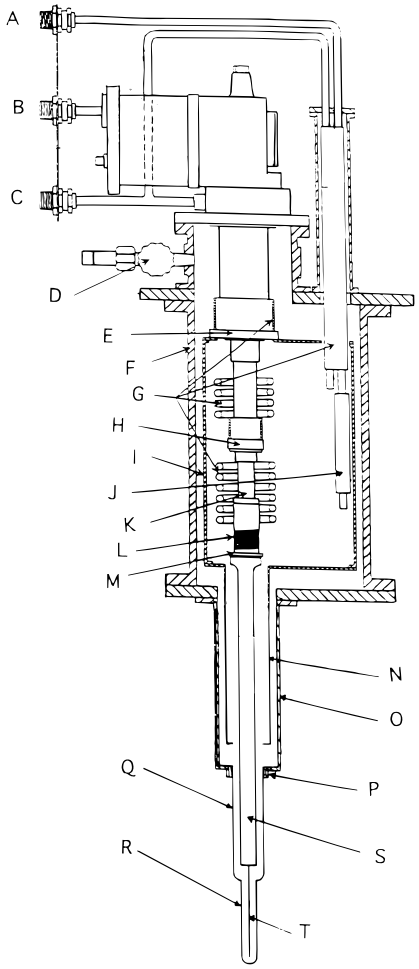


**Figure 1.** Schematic of the cryogenic cold head: (A) Joule−Thomson loop helium return; (B) helium return; (C) helium supply; (D) vacuum shroud pump-out valve; (E) first stage; (F) upper vacuum shroud; (G) heat exchangers; (H) second stage; (I) upper radiation shield; (J) adsorber; (K) thermal switch; (L) heater circuit; (M) third stage; (N) lower radiation shield; (O) lower vacuum shroud; (P) $^{3}/_{4}$ in. Cajon fitting; (Q) $^{3}/_{4}$ in. outer diameter glass tubing; (R) 10 mm NMR tube; (S) oxygen-free high-conductivity (OFHC) copper rod; (T) sapphire rod.

The coil is mounted onto a form made of Kel-F. A seating pattern for the saddle coil is inscribed into the outer wall of the coil form, and 20 gauge copper wire is pressed into this, allowing for very even and closely spaced turns in the coil while also providing a mechanism to support and center the coil in the probe. The wall thickness of the coil form is approximately 0.050 in. The probe body is constructed from an aluminum tube, o.d. = 4.25 in., that has been machined slightly so that it slides easily into a protective aluminum cylinder, i.d. = 4.25 in., placed in the magnet bore.

The spectrometer system is a Varian VXR-200 system with an Oxford horizontal bore magnet. The magnet has a 150 mm bore diameter into which the room-temperature shims are fitted. The protective aluminum cylinder with an i.d. of 4.25 in. is then suspended in the center of the shim bore. This tube is centered in the magnet bore with the aid of a holder mounted on an adjustable-height table in the front of the magnet and an adjustable-height support at the rear of the magnet. Both the table and the rear tube support are attached to the magnet legs as a means of stability. The Varian spectrometer is equipped

with two AR (Amplifier Research) model 1000LM8 broad-band amplifiers, capable of producing 1000 W continuous or 2500 W pulsed power in the frequency range of 1−220 MHz. The output of the observed channel uses a 60 MHz low-pass filter (KW Engineering) along with a 200 MHz notch filter, while the decoupler channel output has two 200 MHz high-pass filters (Eagle, HLC-700 series) in series.

The cryogenic cold head is mounted onto a nonmagnetic track with a screw mechanism (Velmex Unislide track, A6000 series; 6 ft long) that is attached to a table in front of the magnet. By manually turning the screw drive, the cold-head unit can be moved along the axis of the magnet. The probe is first placed in the magnet bore at the proper depth; then the coldfinger is inserted such that the sample is at the optimum position in the rf coil using this screw drive.

### Quantum Mechanical Calculations

DFT (density functional theory) calculations of the chemical-shielding tensor are performed with the Gaussian 94 computer program.[11] All calculations employ the GIAO[12] (gauge including atomic orbitals) method with the D95 basis set[13] for carbons and hydrogens and the Los Alamos ECP plus DZ basis for iron.[14] The DFT calculations use the BLYP exchange-correlation functional[15,16] and a coupled perturbative scheme without including the magnetic field effects in the exchange-correlation functional.[17] Calculations are performed for several different geometries, as discussed in the Results section. The calculated chemical shieldings are converted to the TMS-shift scale by subtracting the TMS shielding value of 186.7 ppm, which is estimated from the calculated value for methane, 193.7 ppm, minus the 7 ppm difference between the experimental chemical shieldings of methane and TMS reported in the literature.[18] The molecular orbitals used in the discussion of the orientation of the principal-axis system were obtained using the Dmol program in the MSi molecular modeling package.[19]

### Results and Discussion

Ferrocene is known to exist in three different solid phases.[20,21] The room-temperature, monoclinic phase, stable to about 164 K, is orange, while a yellow triclinic phase exists below 164 K. More recently, a third low-temperature, greenish orthorhombic phase has been found; this phase is obtained upon crystallization at temperatures below 110 K and exists at temperatures up to approximately 250 K, at which point it transforms directly into the monoclinic phase. The three phases also differ in terms of their degree of order about the long axis of the molecule, with the high-temperature monoclinic phase exhibiting disorder, the intermediate-temperature triclinic phase possessing $D_5$ symmetry with the two cyclopentadienyl rings deviating from being eclipsed by about 10°, and the lowest temperature orthorhombic phase having an eclipsed $D_{5h}$ structure. In the gas phase, the two cyclopentadienyl rings of ferrocene are also eclipsed. Aside from the change in the relative orientation of the two cyclopentadienyl rings, the molecular geometries in the various phases are not very different.

The spectra of ferrocene obtained at room temperature and the lowest temperature (approximately 9 K) are shown in Figure 2, along with several spectra taken at intermediate temperatures, showing the onset of motion as observed in the line shape. All the spectra shown in the figure were recorded on the same sample. The spectra recorded at 9, 15, and 25 K are essentially identical, and the fit of these three spectra all produce the same principal values, within ±3 ppm. The average of the principal values for these three spectra is given in Table 1 along with the data obtained from the fit of the room-temperature spectrum and the literature room-temperature data. The ferrocene sample is orange at room temperature, indicating the monoclinic phase, but when held at 77 K during freeze−pump−thaw cycling to degas the sample and when on the coldfinger of the cryostat at 9 K, the sample turns a bright yellow, suggesting the presence of the triclinic phase. By recording the $^{13}$C powder patterns as a function of temperature, the onset of motion was observed in the vicinity of 45−50 K. At this point, the sample is still yellow. The greenish color associated with the orthorhombic phase was never observed in our experiments. This is not surprising as the pure orthorhombic phase has only been formed by crystallization at a temperature below 110 K.[20] However, the inhomogeneous broadening observed on the high-chemical-shift side of the low-temperature spectrum may indicate the presence

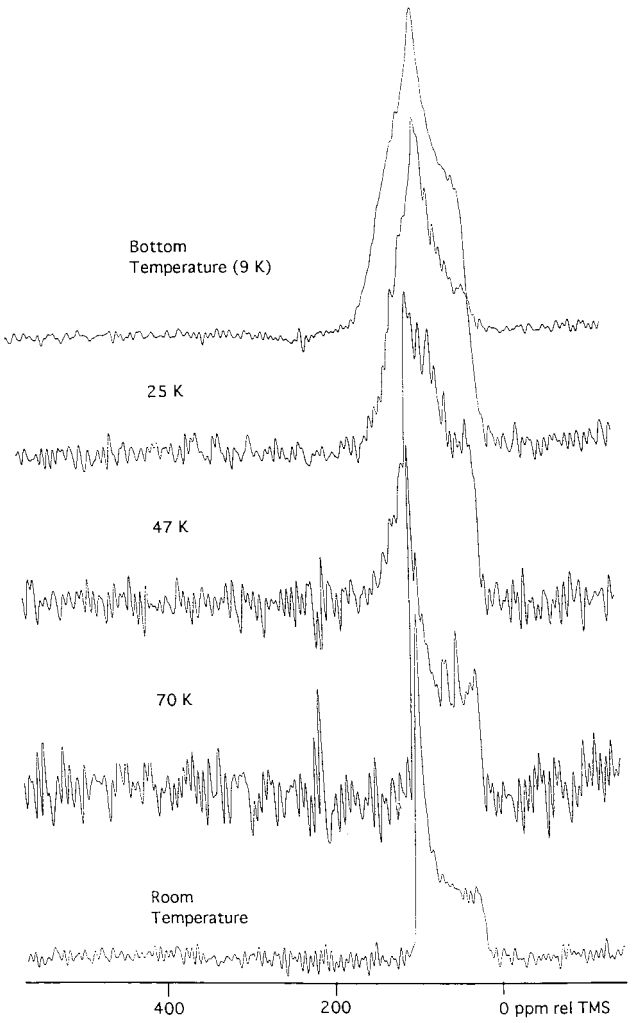


**Figure 2.** $^{13}$C NMR spectra of ferrocene at (a) the bottom temperature of the cryostat (estimated to be 9 K), (b) 25 K, (c) 45 K, (d) 70 K, and (e) room temperature.

**TABLE 1: Experimental Principal Values of the $^{13}$C Chemical-Shift Tensor of Ferrocene[a]**

| | $\delta_{11}$ | $\delta_{22}$ | $\delta_{33}$ | $\delta_{avg}$ |
|---|---|---|---|---|
| RT, this work | 96 | 96 | 18 | 70 |
| RT, literature[b] | 94 | 94 | 18 | 69 |
| RT, literature[c] | 94 | 94 | 17 | 68 |
| LT | 121 ± 3 | 71 ± 2 | 13 ± 2 | 68 ± 2 |

[a] All values reported in ppm on the TMS scale. [b] The values reported in ref 8. [c] Values reported in ref 9.

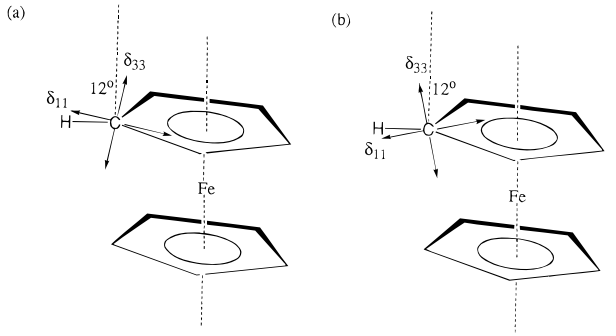


**Figure 3.** Orientation of the principal components of $^{13}C$ chemical-shift tensor in ferrocene, with the $\delta_{22}$ component being perpendicular to the H−C−Fe plane. Experimentally there are two possible orientations (a and b) as the sign of the angle is not determined. Quantum chemical calculations of the chemical-shift tensor, however, predict the orientation given in 3a.

of different crystal forms in the sample. It should be noted that this type of broadening has not been observed on spectra of other compounds recorded using this cryogenic equipment. In addition, low-temperature spectra of ferrocene were recorded using several different samples, and in each case, this broadening was observed. Therefore, the broadening is believed to be due only to the sample and is not an instrumental artifact.

The principal values obtained from the nonrotating ferrocene can be compared with those obtained for the cyclopentadienyl ion (182, 114, and 21 ppm).[22] While the values of $\delta_{33}$ are similar, there are large decreases (61 ppm in $\delta_{11}$ and 33 ppm in $\delta_{22}$) in the two components which generally lie in the plane of the aromatic ring. This is a clear indication that the bonding between the cyclopentadienyl ligand and the central Fe atom greatly decreases the aromatic character of the ring by localizing the $\pi$-electrons into the region of the C−Fe bonding.

The fact that $\delta_{33}$ in the low-temperature case is not the same as $\delta_{||}$ in the room-temperature case indicates that the direction of $\delta_{33}$ does not coincide with the rotation axis. The averaged components are related to the principal components by[23]

$$\delta_{\perp} = {}^1/_2\,(1 - \cos^2\theta \sin^2\phi)\delta_{11} + {}^1/_2\,(1 - \sin^2\theta \sin^2\phi)\delta_{22} + {}^1/_2\,(\sin^2\phi)\delta_{33}$$

$$\delta_{||} = (\cos^2\theta \sin^2\phi)\delta_{11} + (\sin^2\theta \sin^2\phi)\delta_{22} + (\cos^2\phi)\delta_{33}$$

where the polar angles ($\theta$,$\phi$) relate the rotation axis to the principal-axis system of the chemical-shift tensor. Assuming one of the components is perpendicular to the H−C−Fe plane, as required by symmetry if the molecule is in either the staggered or the eclipsed conformation, and assuming this component is $\delta_{22}$, as found for other protonated carbons in aromatic systems,[24,25] it is found that $\delta_{33}$ is oriented at 12.4° ± 0.7° relative to the rotation axis. This value is consistent with the 19° angle measured previously for permethylferrocene.[8] The sign of this angle may not be experimentally determined, resulting in two possible orientations, as shown in Figure 3. Calculations of the chemical-shift tensor, as discussed below, can be used to select the sign of the angle, as well as to explore the validity of the two assumptions made in the above argument.

To determine the effect the different geometries of the various solid phases have on the chemical-shift tensor, calculations were performed using the ordered (refinement B) and disordered (refinement C) structures obtained by neutron diffraction studies at 173 K[26] for the monoclinic form of ferrocene, the X-ray diffraction of the triclinic form at 101 K,[27] the X-ray structure of the orthorhombic form at 98 K,[20] and the gas-phase electron diffraction geometry.[28] The principal values obtained in these calculations are reported in Table 2. The average over all the carbons is given for the triclinic and monoclinic forms as the carbons are magnetically inequivalent. In the higher symmetry of both the orthorhombic phase and the gas phase, all 10 carbons are equivalent. Calculations of the chemical-shielding tensors were also performed on optimized structures, locking the cyclopentadienyl rings in the exactly eclipsed or exactly staggered conformation. The same method and basis set used in the calculation of the chemical shifts was used in the geometry optimizations. The eclipsed-optimized structure was slightly lower (3.6 kJ/mol) in energy, in agreement with the findings of the electron diffraction study[28] as well as a recent DFT theoretical study of metallocenes.[29] In both optimized structures, all of the carbons are equivalent. The optimized geometrical parameters are in good agreement with the experimental values from the literature. The DFT calculations reproduce quite well the geometrical parameters defining the ferrocene geometry, including the Fe−C distance (calculated, 2.12 Å for the eclipsed structure and 2.13 Å for the staggered structure; experimental, 2.01−2.06 Å), which is strongly dependent on the inclusion of electronic correlation effects in the calculations.[30]

**TABLE 2: Calculated Principal Values of the $^{13}C$ Chemical-Shift Tensor of Ferrocene for Different Geometries**

| | $\delta_{11}$ | $\delta_{22}$ | $\delta_{33}$ |
|---|---|---|---|
| experimental | 121 | 71 | 13 |
| isolated structures | | | |
| gas-phase electron diffraction | 123 | 73 | 12 |
| optimized geometry (eclipsed) | 129 | 73 | 14 |
| optimized geometry (staggered) | 129 | 74 | 14 |
| monoclinic | | | |
| (173 K, neutron diffraction, ref B) | 114 ± 6 | 62 ± 1 | 4 ± 9 |
| (173 K, neutron diffraction, ref C) | 117 ± 6 | 62 ± 9 | 5 ± 6 |
| triclinic | | | |
| (101 K, X-ray diffraction) | 118 ± 2 | 61 ± 3 | 2 ± 3 |
| orthorhombic | | | |
| (98 K, X-ray diffraction) | 120 | 68 | 9 |

From the data in Table 2, it is obvious that the chemical-shift values are sufficiently similar to prevent any judgments about the phase of ferrocene that exists on the cold tip. This might be expected as the differences between the various geometries were minor. The calculated principal values, especially for the electron diffraction results, are in good agreement with those measured from the low-temperature spectrum.

The different calculations all specified a similar orientation of the principal-axis system. The calculations indicate that $\delta_{22}$ lies tangential to the ring or perpendicular to the local H−C−Fe plane, supporting the assumption discussed above. The calculated departure of the $\delta_{11}$ component from the C−H direction or of the $\delta_{33}$ component from the rotation axis is between 11° and 15°, in good agreement with the experimental value of 12°. Even though we are uncertain as to the form that exist on the coldtip, the calculations can, therefore, provide the basis for the determination of the direction of the rotation, information not available from the experimental results. All geometries reported in Table 2 predict the orientation shown in Figure 3a, in contrast to a suggestion in the literature for the case of permethylferrocene.[8] The excellent agreement between the experimental and calculated principal values gives credence to the calculated orientation of $\delta_{33}$.

A look at the molecular orbitals can help explain the calculated orientation of $\delta_{11}$ and $\delta_{33}$. To obtain a simplified set of orbitals, additional calculations were performed using the

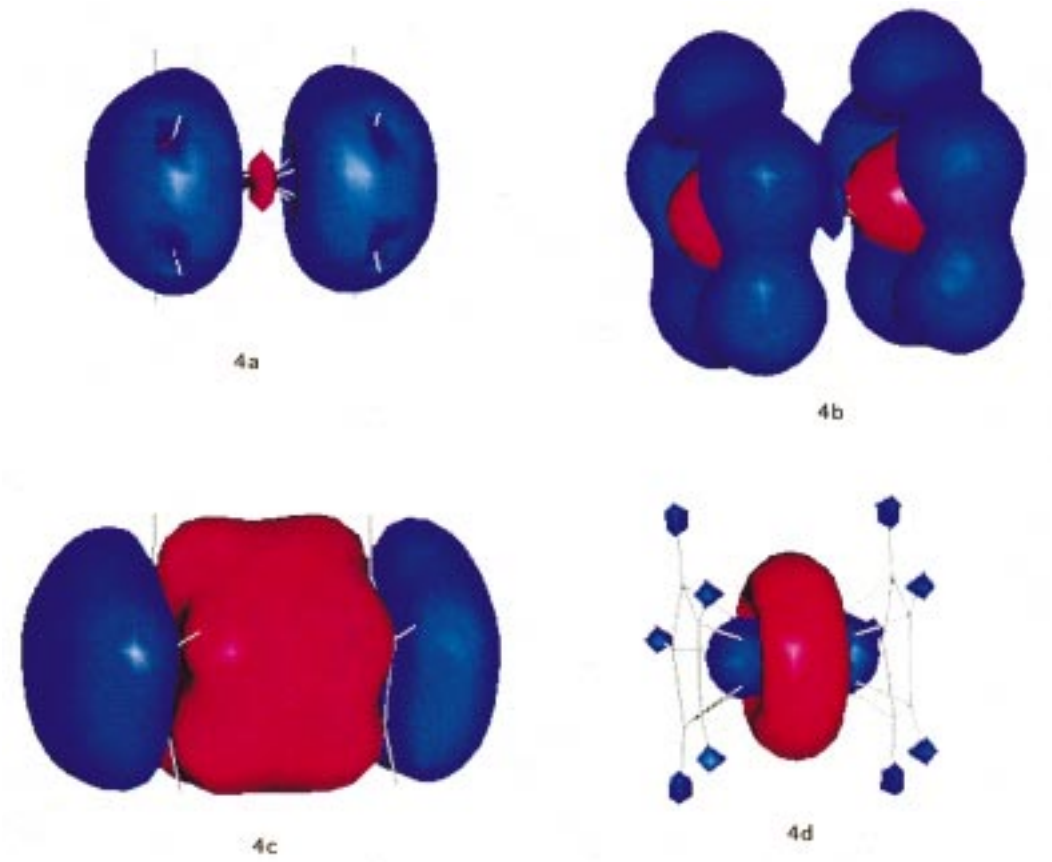


**Figure 4.** Four bonding molecular orbitals of the proper symmetry ($A_1'$ group) to influence the orientation of the $\delta_{11}$ and $\delta_{33}$ components.

**TABLE 3: Atomic Orbital Coefficients of the Molecular Orbitals of A1′ Symmetry**[a]

| | a | b | c | d |
|---|---|---|---|---|
| Fe, 4s | −0.1984 | 0.0025 | −0.1200 | −0.2165 |
| Fe, $3d_0$ | −0.0611 | 0.1264 | 0.0724 | −0.9775 |
| C, 2s | 0.5686 | 0.3806 | 0.1281 | −0.0610 |
| C, $2p_\sigma$ | −0.2773 | 0.6166 | −0.0836 | 0.1087 |
| C, $2p_\pi$ | 0.1434 | −0.0501 | −0.6483 | 0.0315 |
| H, 1s | −0.0794 | −0.2439 | −0.0121 | −0.2004 |

[a] Designation of molecular orbitals as a, b, c, and d refers to Figure 4.

MSi molecular modeling package. Four occupied molecular orbitals of the proper symmetry to contribute to the $\delta_{11}$ and $\delta_{33}$ components exist. The atomic orbital coefficients for these orbitals are reported in Table 3, and pictorial representations of these orbitals are given in Figure 4. The $d_0$ atomic orbital of the iron is along the 5-fold symmetry axis, and the $p_\pi$ orbital of the carbon atom is the p orbital which lies parallel to the $d_0$ iron orbital and is involved in the $\pi$-bonding. Of these four molecular orbitals, the orientation of the $\delta_{11}$ component is dominated by the one shown in Figure 4c as it is the only molecular orbital with appreciable electron density contained in the carbon $p_\pi$ orbital. The interaction between the aromatic ring and the Fe atom leads to a distortion of the nodal symmetry plane in the region of the cyclopentadienyl ring. This mixing of the $p_\pi$ and $p_\sigma$ orbitals of the carbon atoms in the rehybridization process distorts the nodal plane associated with the $\pi$-electrons of the five-membered ring such that it is a slightly concave surface that tilts the $\delta_{11}$ from the plane of the cyclopentadienyl carbons. In typical aromatic systems, it has always been found that the $\delta_{11}$ component lies in the nodal plane of the $\pi$-system and, conversely, the $\delta_{33}$ component lies perpendicular to this nodal plane. In this case, the curvature of the nodal surface explains why the orientation of the $\delta_{11}$ and $\delta_{33}$ components are as shown in Figure 3a. The other three molecular orbitals in Figure 4 will also have an effect on the orientation of the components, but their effects are smaller. Using perturbation theory,[31,32] the effect of a lower energy such as that found for the molecular orbital shown in Figure 4a will decrease the contribution to the paramagnetic term. The electron population of the p orbitals in the molecular orbitals shown in parts b and d of Figure 4 is sufficiently reduced such that these contributions to the chemical shift are, therefore, dominated by the molecular orbital in Figure 4c.

## Conclusions

The principal values of the chemical-shift tensor are reported for ferrocene at several different temperatures. On the NMR time scale, the results indicate that ferrocene stops rotating about its highest symmetry axis at a temperature in the vicinity of 45−50 K. By comparison of the experimental principal values obtained for static ferrocene and rotating ferrocene, the principal axis of the $\delta_{33}$ component is at an angle of ±12° relative to the rotation axis, presuming that the component perpendicular to the Fe−C−H plane is the $\delta_{22}$ component, as indicated by theory.

DFT calculations of the $^{13}C$ chemical-shift tensors produce reasonable results for any of the geometries of ferrocene used in this study, and therefore, the use of the calculations in combination with the powder studies presented here fail to provide any additional insights on the structure of ferrocene present in the experiment. This question can possibly be addressed by single-crystal NMR studies of the three different solid-state phases. However, the calculations still support the finding that the $\delta_{22}$ component is perpendicular to the Fe−C−H plane and further discriminate between the two possible angular orientations of $\delta_{11}$ and $\delta_{33}$ based on the experimental data. This

result suggests that these two components are rotated by approximately 12° from the rotation axis, in the direction indicated in Figure 3a. An analysis of the molecular orbitals provides an explanation for the calculated orientation and indicates which molecular orbital is most likely to be the primary determinant of this orientation.

**Acknowledgment.** This work was funded by the National Science Foundation under Grant No. CHE9006357 and the Department of Energy, Basic Energy Sciences, through Grant No. DE-FG02-94ER14452. Computer resources were provided by the Center for High Performance Computing at the University of Utah.

## References and Notes

(1) Zilm, K. W.; Conlin, R. T.; Grant, D. M.; Michl, J. *J. Am. Chem. Soc*. **1980**, *102*, 6672.
(2) Carduner, K.; Villa, M.; White, D. *Rev. Sci. Instrum*. **1984**, *55*, 68.
(3) Espidel, J. E.; Harris, R. K. *Magn. Reson. Chem*. **1990**, *28*, S15.
(4) McNamara, R.; Wu, C. H.; Opella, S. J. *J. Magn. Reson.* **1992**, *100*, 559.
(5) Macho, V.; Kendrick, R.; Yannoni, C. S. *J. Magn. Reson.* **1983**, *52*, 450.
(6) Doty Scientific, 700 Clemson Road, Columbia, SC 29223.
(7) Kubo, A.; Ikeda, R.; Nakamura, D. *Chem. Lett*. **1981**, 1497.
(8) Wemmer, D. E.; Pines, A. *J. Am. Chem. Soc.* **1981**, *103*, 34.
(9) Hughes, C. D.; Sherwood, M. H.; Alderman, D. W.; Grant, D. M. *J. Magn. Reson., Ser. A* **1993**, *102*, 58.
(10) Jiang, Y. J.; Pugmire, R. J.; Grant, D. M. *J. Magn. Reson.* **1987**, *71*, 485.
(11) Frisch, M. J.; Trucks, G. W.; Schlegel, H. B.; Gill, P. M. W.; Johnson, B. G.; Robb, M. A.; Cheeseman, J. R.; Keith, T. A.; Petersson, G. A.; Montgomery, J. A.; Raghavachari, K.; Al-Laham, M. A.; Zakrzewski, V. G.; Ortiz, J. V.; Foresman, J. B.; Cioslowski, J.; Stefanov, B. B.; Nanayakkara, A.; Challacombe, M.; Peng, C. Y.; Ayala, P. Y.; Chen, W.; Wong, M. W.; Andres, J. L.; Replogle, E. S.; Gomperts, R.; Martin, R. L.; Fox, D. J.; Binkley, J. S.; Defrees, D. J.; Baker, J.; Stewart, J. P.; Head-Gordon, M.; Gonzalez, C.; Pople, J. A. *Gaussian 94*, Revision A.1; Gaussian, Inc.: Pittsburgh, PA, 1995.
(12) Ditchfield, R. *Mol. Phys.* **1974**, *27*, 789.
(13) Dunning, T. H.; Hay, P. J. In *Modern Theoretical Chemistry*; Schaefer, H. F., III, Ed.; Plenum: New York, 1976; p 1.
(14) Hay, P. J.; Wadt, W. R. *J. Chem. Phys.* **1985**, *82*, 270, 284, and 299.
(15) Lee, C.; Yang, W.; Parr, R. G. *Phys. Rev.* **1988**, *B37*, 785.
(16) Becke, A. D. *Phys. Rev.* **1988**, *A38*, 3098.
(17) Cheeseman, J. R.; Trucks, G. W.; Keith, T. A.; Frisch, M. J. *J. Chem. Phys.* **1996**, *104*, 5497.
(18) Jameson, A. K.; Jameson, C. J. *Chem. Phys. Lett.* **1987**, *134*, 461.
(19) Molecular Simulations: San Diego, CA, 1996.
(20) Seiler, P.; Dunitz, J. D. *Acta Crystallogr*. **1982**, *B38*, 1741.
(21) Calvarin, G.; Clec′h, G.; Berar, J. F.; Andre, D. *J. Phys. Chem. Solids* **1982**, *43*, 785.
(22) Strub, H.; Beeler, A. J.; Grant, D. M.; Michl, J.; Cutts, P. W.; Zilm, K. W. *J. Am. Chem. Soc.* **1983**, *105*, 3333.
(23) Mehring, M. *NMR: Basic Principles and Progress*: Springer Verlag: Heidelberg, 1983; p 50.
(24) Iuliucci, R. J.; Phung, C. G.; Facelli, J. C.; Grant, D. M. *J. Am. Chem. Soc*. **1996**, *118*, 4880 and preceding papers in series.
(25) Facelli, J. C.; Grant, D. M. *Theor. Chim. Acta* **1987**, *71*, 277.
(26) Takusagawa, F.; Koetzle, T. F. *Acta Crystallogr*. **1979**, *B35*, 1074.
(27) Seiler, P.; Dunitz, J. D. *Acta Crystallogr*. **1979**, *B35*, 2020.
(28) Haaland, A.; Nilsson, J. E. *Acta Chem. Scand.* **1968**, *22*, 2653.
(29) Matsuzawa, N.; Seto, J.; Dixon, D. A. *J. Phys. Chem. A* **1997**, *101*, 9391.
(30) Koch, H.; Jorgensen, P.; Helgaker, T. *J. Chem. Phys*. **1996**, *104*, 9528.
(31) Ramsey, N. F. *Phys. Rev.* **1950**, *77*, 567.
(32) Ramsey, N. F. *Phys. Rev.* **1950**, *78*, 699.